Joule

CellPress

Report

Synergistic Tandem Solar Electricity-Water Generators

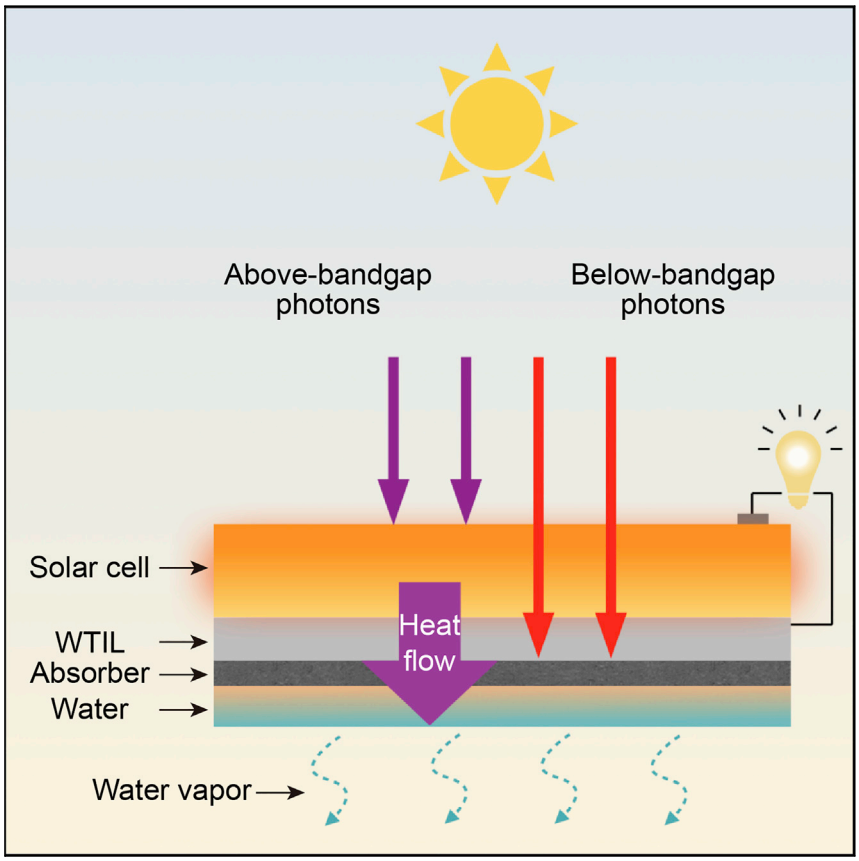

Energy and clean water are two intertwined fundamental elements for human civilization and sustainable development. This work demonstrates a monolithic tandem solar electricity-water generator that synergistically produces electricity and clean water by utilizing the full spectrum of solar irradiance. The two components, the top infrared photovoltaic device and the bottom water purifier, mutually benefit each other. This tandem device not only serves as a portable life-supporting system but also provides a promising integrated alternative for utility-scale electricity generation and water purification.

Ning Xu, Pengchen Zhu, Yun Sheng, ..., Hairen Tan, Shining Zhu, Jia Zhu

hairentan@nju.edu.cn (H.T.)
jiazhu@nju.edu.cn (J.Z.)

HIGHLIGHTS

Electricity and clean water are produced simultaneously under sunlight

The top solar cell and bottom water purifier mutually benefit each other

The full-spectrum utilization of solar energy is realized

Xu et al., Joule 4, 347–358
February 19, 2020
https://doi.org/10.1016/j.joule.2019.12.010

Joule

CellPress

Report

Synergistic Tandem Solar Electricity-Water Generators

Ning Xu,[1,3] Pengchen Zhu,[1,3] Yun Sheng,[2] Lin Zhou,[1] Xiuqiang Li,[1] Hairen Tan,[1,*] Shining Zhu,[1] and Jia Zhu[1,4,*]

SUMMARY

Energy and clean water are two intertwined fundamental elements for human civilization and sustainable development. Here, we devise a monolithic tandem solar electricity-water generator that synergistically produces electricity and clean water by utilizing the full spectrum of solar irradiance. The tandem generator has two components: a top infrared-transparent photovoltaic device using above-band-gap photons, and a bottom solar water purifier using the below-band-gap photons. More strikingly, a well-designed water-proof thermal interconnecting layer (WTIL) makes these two components work synergistically: the bottom purifier serves as an evaporative cooler of the top solar cell to increase its efficiency, whereas the thermalization energy of the top cell is reutilized by the bottom purifier for producing more clean water. We experimentally demonstrate that a prototype hybrid tandem solar device with WTIL can generate electricity with a power output of 204 W m^{-2} and purify water at a rate of 0.80 kg m^{-2} h^{-1} under 1-sun illumination.

INTRODUCTION

Growing global population and changing climate call for sustainable generation of electricity and clean water, two cornerstones for social development and economic growth.[1–3] Although the nexus of energy and water poses an intertwined challenge to today's society, the technological development of producing green electricity and clean water has been taking independent and separate pathways.[4,5] The two systems of producing power and purified water can be combined using separate infrastructures and landscapes,[6–8] but this inevitably leading to high costs, large footprint areas, and low energy utilization efficiency to achieve both goals.

Tremendous progress has been made in the field of photovoltaics with steadily increased efficiency and reduced cost.[9–12] So far, the efficiency of a single-junction photovoltaic (PV) device is still below 30%, leaving a large portion (>70%) of solar irradiance wasted. The excess energy of above-band-gap photons (after absorption) rapidly dissipates as heat via the thermalization of photo-carriers to band edges (Figure 1A). The below-band-gap photons will either generate heat if they are trapped within the solar cell or pass through without utilization (Figure 1B). The thermalization energy leads to increased cell temperature and deteriorated photovoltaic performance.[13]

In the field of water treatment, significant advancement has been made in terms of both cost and energy efficiency.[14–22] Remarkably, the energy efficiency of reverse osmosis (RO) is approaching the thermodynamic limit.[23] Nevertheless, energy sources and environmental impacts related to powering the desalination plants are still the primary concerns for future development.[24]

Context & Scale

Electricity and clean water are two fundamental elements for daily life. Existing techniques typically produce them independently, leading to high cost and low energy efficiency. Here, we devise a tandem solar electricity-water generator that simultaneously produces electricity and clean water by fully using solar energy. The tandem generator has two components: a top photovoltaic device using high-energy photons, and a bottom solar water purifier using low-energy photons. More strikingly, the two components mutually benefit each other in the integrated system: the bottom purifier can be an evaporative cooler for the top solar cell to increase its efficiency, whereas the thermalization energy of the top cell is reutilized by the bottom purifier for producing more clean water. We experimentally demonstrate that a prototype hybrid tandem solar device can generate electricity with a relative enhancement of 7.9% and purify water at a rate of 0.80 kg m^{-2} h^{-1} under natural sunlight.

Attempts to design integrated systems that could simultaneously generate clean water and electricity from solar illumination have recently seen initial interest.[25,26] Although the solar thermal efficiency in those integrated systems could be as high as stand-alone solar thermal systems, the electricity outputs have been rather limited, below 1 W m^{-2} under 1-sun illumination.

RESULTS AND DISCUSSION

Here, we devise a monolithic tandem solar electricity-water generator that simultaneously produces electricity from the top cell and clean water from the bottom purifier by utilizing full-spectrum solar irradiance. A water-proof thermal interconnecting layer (WTIL) connecting the top and bottom devices enables them to work synergistically. The rational design of the tandem solar electricity-water generator is illustrated in Figure 1C. It consists of two solar generators: a PV cell at the top for electricity generation by absorbing above-band-gap photons, and an interfacial solar water purifier underneath the PV device for clean water generation by utilizing the below-band-gap photons. A WTIL is inserted to tightly connect the two components, in order to ensure the effective transfer of the thermalization energy from the top PV cell to the bottom water purifier (Figure 1C). The WTIL is crucial for the two devices to work synergistically because the top solar cell can be cooled down by the bottom purifier, thereby ensuring improved power conversion efficiency; the bottom water purifier can reutilize the thermalization energy from the top cell (which is otherwise wasted) to purify more water. To evaluate the synergistic effect enabled by WTIL, the performance of tandem systems without and with WTIL will be compared, and the two systems are referred to as separated (Figure 1C, left) and integrated (Figure 1C, right) tandem systems, respectively.

To justify the feasibility of tandem solar electricity-water generators, we experimentally constructed an integrated hybrid tandem device by integrating an infrared-transparent crystalline silicon (Si) PV cell and reduced graphene oxide (r-GO)-based solar water purifier (Figures 1D and 1E). The Si solar cell with grid electrodes on both sides is designed and fabricated to form an infrared-transparent device (Figures S1 and S2), which allows below-band-gap photons to transmit through. These below-band-gap photons can be captured by the underneath r-GO absorber. The two ends of the r-GO absorber are in direct contact with water sources (such as seawater and wastewater) for continuous water supply. The absorbed below-band-gap photons will then be used for interfacial solar evaporation and purification (see more information on interfacial solar evaporation in Experimental Procedures).[14,15,27–38] The hot water vapor is condensed by the cold sidewall of the container and flows downward into the container.

As explained above, the WTIL, which connects the top and bottom cells, is crucial for synergistic operation in the tandem systems. There are two essential requirements for the WTIL. First, it should ensure effective heat transfer from the top cell to the bottom purifier in order to reutilize the thermalization energy for extra water production and to cool down the working temperature of the solar cell. Second, it should be able to protect the solar cell from being degraded by the water vapor generated from the bottom purifier. Ethylene vinyl acetate (EVA) is chosen as it is one of the industry-standard encapsulating materials for silicon solar cells, with well-proven long-term stability.[39] Vertically aligned carbon nanotubes (VACNT) are used for their excellent thermal conductivity and mechanical properties.[40] Therefore, it can be expected that the VACNT-embedded EVA membrane (Figure 2A) with elaborate design should possess the water-proof capability, good thermal conductance, and asymmetric surface properties, which will be examined in detail below. The

[1]National Laboratory of Solid State Microstructures, College of Engineering and Applied Sciences, Jiangsu Key Laboratory of Artificial Functional Materials, Nanjing University, Nanjing 210093, P. R. China

[2]State Key Laboratory of PV Science and Technology, Trina Solar, No. 2 Trina Road, Changzhou 213031, China

[3]These authors contributed equally

[4]Lead Contact

*Correspondence: hairentan@nju.edu.cn (H.T.), jiazhu@nju.edu.cn (J.Z.)

https://doi.org/10.1016/j.joule.2019.12.010

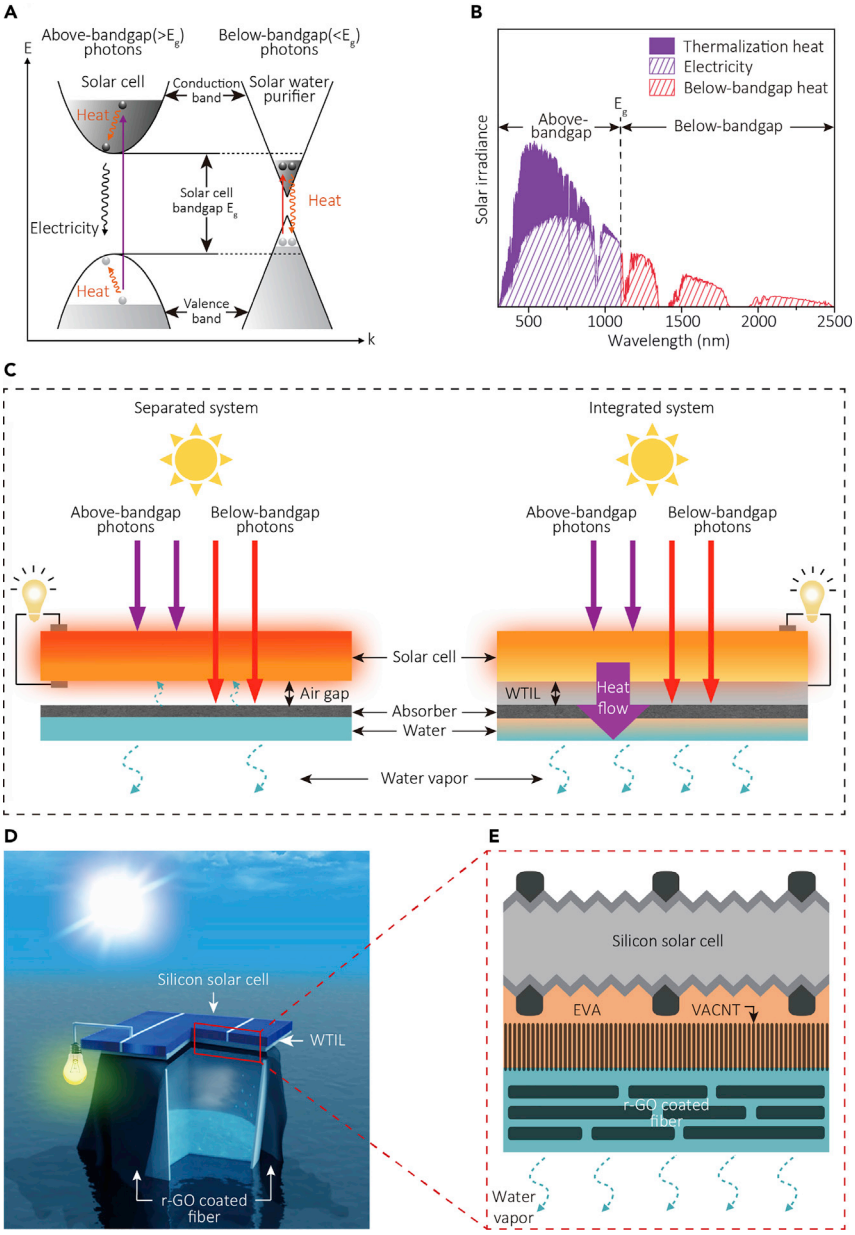

Figure 1. Structure of Monolithic Tandem Solar Electricity-Water Generators

(A) Band diagram of the tandem solar electricity-water generator.

(B) Solar energy utilization in the hybrid tandem device: part of the above-band-gap solar energy for electricity generation (purple grid), thermalization heat from above-band-gap solar energy (purple), and below-band-gap solar energy (red grid) for water vapor generation.

(C) Separated tandem solar electricity-water generator (left) and integrated tandem solar electricity-water generator with synergic effect (right). The top PV cell absorbs above-band-gap photons to produce electricity. The bottom water purifier absorbs below-band-gap photons to produce clean water. For an integrated tandem device, after using a water-proof thermal interconnecting layer (WTIL), thermalization heat generated in the PV cell is transferred to the water purifier, which enhances the water generation and cools down the PV cell.

(D and E) Schematic (D) and device structure (E) of the integrated tandem solar electricity-water generator constructed in this work. An infrared-transparent crystalline silicon (Si) solar cell is deployed as the top PV cell. A reduced graphene oxide (r-GO) based fabric is used for the solar water purifier. A VACNT-embedded ethylene vinyl acetate (EVA) layer serves as WTIL, connecting the cell and the water purifier, to ensure protection of the cell and effective heat transfer. CNT, carbon nanotubes; VACNT, vertically aligned CNT.

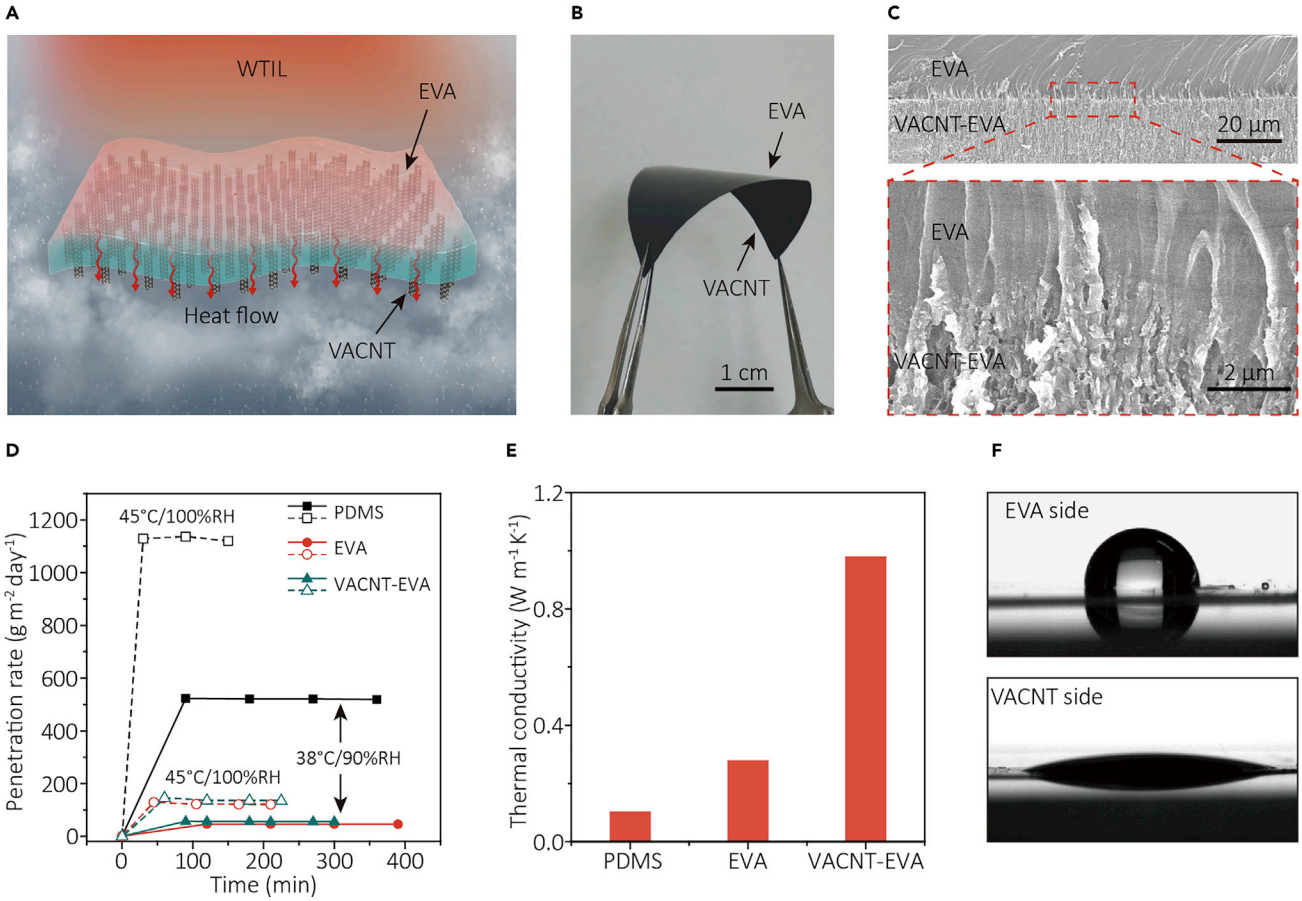

Figure 2. Characterizations of Water-Proof Thermal Interconnecting Layer

(A and B) Schematic (A) and photograph (B) of the VACNT-embedded EVA membrane.

(C) SEM image of the interconnecting layer at the interface of the VACNT and EVA.

(D) Vapor penetration of PDMS, EVA, and VACNT-embedded EVA (VACNT-EVA) membranes. The filled symbol refers to the testing condition with a temperature of 38°C and a relative humidity (RH) of 90%, and the open symbol is for 45°C and 100% RH.

(E) Thermal conductivities of PDMS, EVA, and VACNT-embedded EVA membranes.

(F) Wetting properties of two sides of the VACNT-embedded EVA membrane.

as-fabricated VACNT-embedded EVA membrane is shown in Figure 2B (see fabrication in Experimental Procedures). Figure 2C shows the zoom-in image of the VACNT-embedded EVA membrane (typically 80–90 μm thick).

As shown in Figure 2D, the VACNT-embedded EVA membrane has water vapor penetration rates of 56 g m^{-2} day^{-1} at a humidity of 90% and a temperature of 38°C, and of 135 g m^{-2} day^{-1} at a humidity of 100% and a temperature of 45°C, similar to those of the pure EVA membrane (about 46 g m^{-2} day^{-1} at a humidity of 90% and a temperature of 38°C, and 121 g m^{-2} day^{-1} at a humidity of 100% and a temperature of 45°C). This indicates that the VACNT-embedded EVA membrane reserves excellent water-proof capability. Both VACNT-embedded and pure EVA membranes have a much lower vapor penetration rate than that of the polydimethylsiloxane (PDMS) membrane, a common material widely used for flexible electronics.[41,42] The VACNT-embedded EVA membrane also exhibits better thermal conductance because carbon nanotubes (CNTs) provide channels for heat transfer. As shown in Figure 2E, VACNT-embedded EVA has much higher thermal conductivity (0.98 W m^{-1} K^{-1}) compared with pure EVA (0.28 W m^{-1} K^{-1}) and PDMS

(0.11 W m^{-1} K^{-1}) membrane. The membrane also efficiently captures transmission below-gap photons because of its good broadband absorption (Figure S3) and then transfers this part of energy to the water path in the heat form. It should also be noted that this composite membrane is constructed to have asymmetric wetting properties (Figure 2F) for connecting different parts of the synergistic tandem system. The upper side connecting the top solar cell is electrical-insulating and hydrophobic EVA (contacting angle of ~92°), which protects the solar cell from water vapor generated by the bottom purifier to ensure long-term stability. The lower side mainly consists of hydrophilic CNTs-based materials (plasma-treated, contacting angle of ~15°) for excellent mechanical (Figure S4) and thermal contacts with the bottom purifier.

To evaluate the synergistic effect enabled by WTIL on the overall performance, the tandem systems without and with WTIL were compared and referred to as separated (Figure 3A, left and Figure S5A) and integrated systems (Figure 3A, right and Figure S5B), respectively. For a single-junction PV cell, it is well known that the thermalization energy leads to increased solar cell temperature and thereby reduces the power conversion efficiency (PCE) of PV cells in practical applications.[13] As shown in Figure 3B, the temperature of the stand-alone photovoltaic devices (as the case in the separated system) without any additional cooling can reach 50°C and 62°C under 1.0 and 1.5 kW m^{-2}, respectively. In our integrated tandem system with WTIL, the working temperatures of the top solar cell are 11°C and 18°C lower under 1.0 and 1.5 kW m^{-2} illuminations, compared with that of the separated system, respectively (Figure 3B). This is because the bottom water purifier serves as an evaporative cooler for the PV cell and takes away the thermal heat from the solar cell via the WTIL. As a result of lower working temperature, the PCE of the Si solar cell in the integrated device was 20.4%, higher than that of the separated device (18.9%) under 1.0 kW m^{-2} illumination (Figure 3C; Table 1, and the incident photon-to-electron conversion efficiency (IPCE) data are shown in Figure S6). The PCE enhancement becomes more significant (from 18.0% to 20.2%) under 1.5 kW m^{-2} illumination. Therefore, it is clear that with WTIL for effective heat transfer, the bottom purifier serves as an evaporative cooler, with a cooling power of 367 W m^{-2} under 1.0 kW m^{-2} illumination. The cooling power of this evaporative cooler increases under higher illumination (see more details of measurement and calculation in Experimental Procedures).

In addition to the increased PCE in the PV cell, the integrated system exhibits enhanced water vapor generation for the purifier (Figure 3D). The net evaporation rates and conversion efficiencies of the integrated device increase by about three times compared with performances of the separated device (from 0.12 to 0.39 kg m^{-2} h^{-1} and 16.5% to 53.3% under 0.5 kW m^{-2} h^{-1}, from 0.26 to 0.80 kg m^{-2} h^{-1} and 17.5% to 54.2% under 1 kW m^{-2}, and from 0.44 to 1.25 kg m^{-2} h^{-1} and 20.1% to 56.8% under 1.5 kW m^{-2}, respectively). The mutual enhancement of electricity and water generation under different solar illuminations are summarized in Figures 3E and 3F (see more calculation details for net evaporation rates and conversion efficiencies in Experimental Procedures).

To explicitly evaluate the utilization of thermalization heat for water vapor generation, we placed a 1,100-nm cutting-off optical filter in front of the top solar cell to select above-band-gap photons only (Figure S7). The curves of net mass changes of the system with the filter under various illumination conditions (0.5, 1.0, and 1.5 kW m^{-2}) are shown in Figure S8A. The net evaporation rates and energy conversion efficiencies of thermalization heat under illuminations of 0.5, 1.0, and 1.5 kW m^{-2} are 0.24, 0.50,

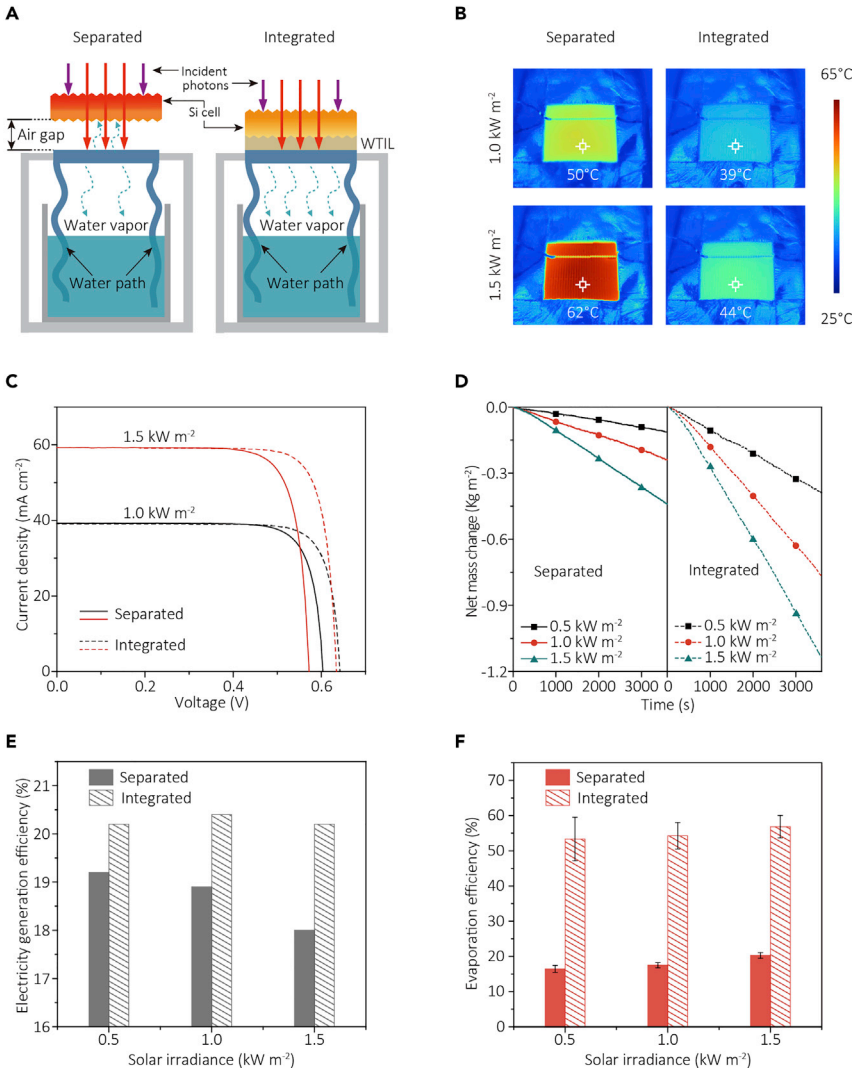

Figure 3. Performances of the Integrated Tandem Solar Electricity-Water Generator for Mutually Enhanced Electricity and Water Generation

(A) Schematics of the separated (left) and integrated (right) tandem solar generator.

(B) Solar cell temperatures of the separated and integrated system under illuminations of 1.0 and 1.5 kW m^{-2}.

(C) Photovoltaic performances of the Si solar cell in separated and integrated systems under illuminations of 1.0 and 1.5 kW m^{-2}.

(D) Net mass changes over time under different illuminations.

(E) Summary of the performances of the electricity generation in separated and integrated systems under illuminations of 1.0 and 1.5 kW m^{-2}, respectively.

(F) Summary of the performances of the solar water purifier in separated and integrated systems under illuminations of 1.0 and 1.5 kW m^{-2}, respectively. The error bars denote standard deviations, obtained by multiple experimental measurements.

and 0.78 kg m^{-2} h^{-1} and 33.3%, 34.0%, and 35.4%, respectively, as presented in Figure S8B (see more calculation details in Experimental Procedures).

The monolithic synergistic tandem solar electricity-water generation system has promising potential as a portable life-supporting system, which can provide both electricity and clean water in remote areas (Figure 4A). To verify the performance

Table 1. Photovoltaic Performance of Solar Cell in Separated and Integrated Systems under Different Solar Irradiances

Power Density (kW m^{-2})	Condition	V_{oc} (V)	J_{sc} (mA cm^{-2})	FF (%)	PCE (%)
1.0	separated	0.603	39.1	80.5	18.9
	integrated	0.641	39.1	81.5	20.4
1.5	separated	0.573	59.2	79.5	18.0
	integrated	0.634	59.1	80.8	20.2

under continuous illumination, the output of electricity and water purification over time under various illumination intensities are presented in Figure 4B. We also performed a stability test of our tandem device with a 3.5% salt water source, showing steady production of electricity and water for over 120 h (Figure S9). The overall energy flow under sunlight of 1.0 kW m^{-2} in this integrated tandem generator system is illustrated in Figure 4C. It is capable of utilizing 74.6% of the whole solar energy (20.4% for solar electricity and 54.2% for solar water vapor) in our practical prototype tandem device. Another ~15% of non-utilized solar energy includes optical reflection loss (~11%) (Figure S10) and heat losses due to radiation and convection, which leaves room for future development (more analytical details can be found in Experimental Procedures).

The solar water purifier is capable of purifying various kinds of water resources. Three typical water sources (seawater, industrial wastewater, and bacteria-contaminated water) were investigated herein as examples. For seawater (from the Bohai Sea, China), the concentrations of four primary ions (Na^+, Mg^{2+}, Ca^{2+}, and B^{3+}) after desalination were reduced by at least three orders of magnitude and all reached the World Health Organization (WHO) standards for drinking water (Figure 4D).[43] For industrial wastewater (five heavy metals ions with different concentrations 300 mg L^{-1} Ni^{2+}, 300 mg L^{-1} Cu^{2+}, 300 mg L^{-1} Pb^{2+}, 100 mg L^{-1} Cr^{3+} and 100 mg L^{-1} Zn^{2+}), all heavy metal ions were also purified well by our device, and the concentrations after purification for all reached WHO standards for drinkable water (Figure 4E). For the bacteria-contaminated water (contaminated by *Escherichia coli* [*E. coli*] and *Staphylococcus aureus* [*S. aureus*]), both bacteria *E. coli* and *S. aureus* in the contaminated water were effectively removed after purification (Figure 4F).

On the utility-scale, this hybrid tandem solar-conversion device can add much more value to large-scale solar plants by increasing the electricity generation and purifying water without extra infrastructures and landscapes. For example, by replacing a 1-MW photovoltaic plant with our tandem solar electricity-water device, each day we can purify 24 tons of water and produce 480 kWh more electricity (assuming 6 sun-h per day, see more details of the calculation in Experimental Procedures).[44]

In summary, we devised a monolithic hybrid tandem solar electricity-water generator device for synergetic electricity generation and water purification with full solar spectrum utilization and high conversion efficiencies. We experimentally constructed a prototype hybrid tandem solar device that could generate electricity with a power output of 204 W m^{-2} and purify water at a rate of 0.80 kg m^{-2} h^{-1} under 1-sun illumination, representing an overall solar energy utilization efficiency of 74.6%. It is expected that advances in PV devices, interfacial solar evaporation, and water-proof thermal interconnecting materials could lead to tandem generators with even higher efficiency and lower cost.[32,45,46] The hybrid tandem solar

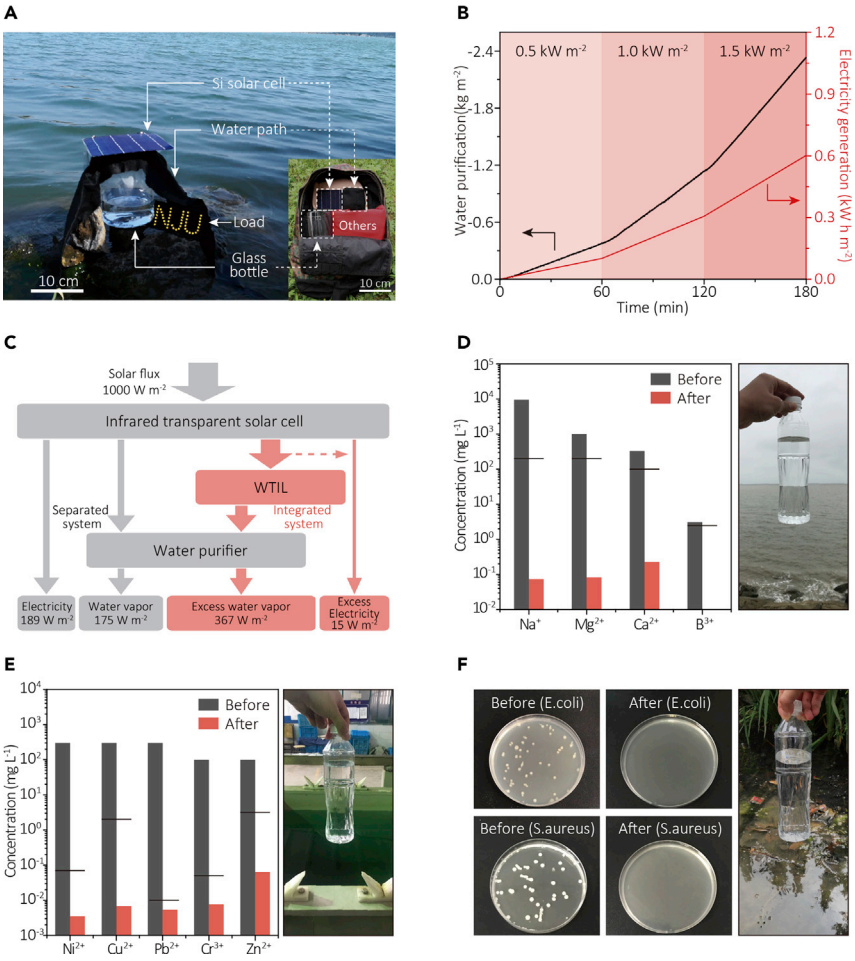

Figure 4. Continuous Working Performance, Energy Flow, and Water Quality out of the Integrated Tandem Solar Electricity-Water Generator

(A) Photograph of a portable tandem solar generator for outdoor application. The inset: the entire device occupies a small volume of a common backpack.

(B) Continuous working performances of simultaneous electricity production and water purification under various illumination intensities.

(C) Detailed analysis of the energy flows in the hybrid tandem device. WTIL enables a synergistic effect, which produces more water and electricity.

(D) Concentrations of four primary ions (Na^+, Mg^{2+}, Ca^{2+}, and B^{3+}) in a seawater sample (from the Bohai Sea, China; average salinity ~1 wt %) before and after desalination. The black lines show the WHO standard of ion concentrations for drinking water. The B^{3+} ions cannot be detected by ICP after purification.

(E) Concentrations of five classical ions in a simulated industrial wastewater sample (300 mg L^{-1} Ni^{2+}, 300 mg L^{-1} Cu^{2+}, 300 mg L^{-1} Pb^{2+}, 100 mg L^{-1} Cr^{3+}, and 100 mg L^{-1} Zn^{2+}) before and after purification. The black lines show the WHO standard of ion concentrations for drinking water.

(F) The concentrations of bacteria *E. coli* (top) and *S. aureus* (bottom) before and after purification are demonstrated in the left and right plates, respectively.

electricity-water generator not only provides a complementary and portable solution for sustainable supply of electricity and drinking water in off-grid areas but also offers a feasible solution for utility-scale electricity generation and water purification in resource-stress regions. For example, the thermal interfacial layer is being highly pursued, and it is expected that the community will find more material systems to meet the large-scale requirements in terms of performance and cost. Our tandem device can also help to improve the overall performance of PV plus RO

systems[47,48] by providing extra water (increased yield of 0.80 kg m^{-2} h^{-1} under 1-sun illumination) as well as extra electricity (a relative enhancement of 7.9% under 1-sun illumination), which can also be used to power RO systems for clean water production (for details, see Experimental Procedures).

EXPERIMENTAL PROCEDURES

Fabrication of Infrared-Transparent Si PV Cell

A 180-μm-thick p-type silicon wafer was textured in a potassium hydroxide solution to produce random pyramids on both sides.[49] The p^+ and n^+ layers were then formed by thermal diffusion. An 80-nm-thick SiN_x layer was coated on both sides for effective surface passivation and served as an anti-reflection layer on the front side. Finally, silver grid electrodes were fabricated on both sides by screen printing.

Fabrication of Reduced Graphene-Oxide-Based Solar Water Purifier (r-GO-Coated Fabrics)

Graphene oxide (GO) nanosheets were dispersed in deionized water (3 mg/mL) by ultrasonic vibration for 2 h. Thereafter, the GO solution was sprayed onto the preheated fabrics using a commercial airbrush (Nozzle diameter of 0.3 mm, Ustar CD-601) to produce GO-coated fabrics. The GO coated fabrics (graphene-based fabric) were then baked at 150°C in a vacuum to obtain r-GO-coated fabrics. Scanning electron microscope (SEM) images of fabrics only and r-GO-coated nonwoven fabrics are shown in Figure S11.

Fabrication of Water-Proof Thermal Interconnecting Layer: VACNT-Embedded EVA Membrane

The VACNT was fabricated by a template method.[50,51] The VACNT membrane and EVA membrane with 80–90 μm thick were sandwiched with two Teflon plates. After hot-pressing under 130°C–180°C for 20–60 min in vacuum, the VACNT-embedded EVA membrane was obtained. The VANCT was pre-treated (plasma cleaning) to be hydrophilic. The EVA side of the membrane is bonded with the bottom side of the solar cell by a hot-pressing method. Specifically, the process was conducted under 110°C–130°C as the EVA membrane was melted and a constant pressure about 10^4 Pa was simultaneously loaded on them. The whole hot-pressing process was continued for minutes to ensure a good connection between the solar cell and EVA.

Characterizations

The morphologies and structures of the solar water purifier (r-GO coated fabrics) were characterized by scanning electron microscopy (SEM, FEI, Quanta 200). The absorption spectra of the Si PV cell and r-GO coated fabrics and the transmittance of the Si PV cell were measured from 280 to 2500 nm using a UV/vis/NIR spectrometer (UV-3600, Shimadzu). A FLUKE TiX 580 infrared camera was used to take infrared photographs. Concentrations of ions in brine and clean water were tracked by inductively coupled plasma spectroscopy (ICP–OES, OPTIMA 5300 DV, PerkinElmer Instrument). The J-V curves of silicon solar cells were taken using a source meter (Keithley 2400) and a solar simulator (AM 1.5 G, Newport 94043A, Class AAA). A Newport-calibrated solar cell with a quartz window was used to adjust the light intensity into 1 kW m^{-2}. Typically, the silicon solar cells were measured from +0.7 V to −0.1 V with a voltage step of 10 mV and a delay time of 100 ms. The J-V measurement was taken in the ambient environment (about 40% RH and 26°C). The IPCE spectra were taken by the QEX-10 system without light bias in the ambient environment (about 40% RH and 26°C).

Measurements of Electricity and Vapor Generations

Concave support with upper opening (Figure S5) for evaluating the performance of thermal/solar vapor generation in Figures 3D and 3F, and water purification in Figure 4B: a concave support with upper opening was made by tinfoil, and the central part of the flexible reduced graphene oxide (r-GO) absorber was fixed on the opening with both ends in direct contact with the water container to take up the water. For the integrated tandem system, the silicon solar cell (the same size and shape as the flattened central part) with WTIL was tightly connected with the r-GO absorber. For the separated tandem device, the Si cell without WTIL was placed 3 mm away from the r-GO absorber.

The devices were irradiated by a solar simulator (AM 1.5 G, Newport 94043A, Class AAA). Once the light was on, the output electricity was recorded by a source meter (Keithley 2400) or extracted by an external resistor, and meanwhile, the mass changes of the separated or integrated devices were tracked by a high accuracy balance (FA 2004, 0.1 mg in accuracy) connected to a desktop computer (real-time tracking with RS-232 serial ports. The mass changes we plotted are net mass changes, which means we extracted dark evaporation induced mass changes from the total evaporation under sunlight (Figures 3D and S7A). The net evaporation rates and energy conversion efficiencies are calculated from the slope from the steady states (2000∼3600 s) of the net mass change curves.

Calculations of Conversion Efficiencies

Conversion efficiency (η) is defined as $\dot{m}h_{lv}/P_{solar}$, where $\dot{m}$ is the mass flux of vapor, h_{lv} is the liquid-vapor phase change enthalpy (2450 kJ kg^{-1} for generating vapor of ∼40°C), and P_{solar} is the intensity of solar energy.

Bacterial Experiments

E. coli and *S. aureus* were incubated by lysogeny broth and dispersed in normal saline as bacteria-contaminated water for the purification experiments. We detected water samples before and after purification by plate counting. 100 μL of each sample was plated in triplicate and incubated at 37°C for 24 h. The counting results were shown in Figure 4F (10^5-fold diluted for *E. coli* and 10^4-fold diluted for *S. aureus*). The purified water used for plate counting was not diluted.

SUPPLEMENTAL INFORMATION

Supplemental Information can be found online at https://doi.org/10.1016/j.joule.2019.12.010.

ACKNOWLEDGMENTS

We acknowledge the micro-fabrication center of National Laboratory of Solid State Microstructures (NLSSM) for technical support and Yingying Zou, Jisong Hua, and Zuoxiu Tie for the help with germiculture. We acknowledge Daming Chen and Yifeng Chen for the fabrication of silicon solar cells and Shuai Gu for the outdoor experiment. We also acknowledge Junjie Jiang and Xiaoshan Wu for the IPCE measurement. This work is jointly supported by the National Key Research and Development Program of China (no. 2017YFA0205700)—and the National Natural Science Foundation of China (grant nos.—51925204 and 61735008). H.T. acknowledges the support from the National Thousand Young Talents Award in China and the Fundamental Research Funds for the Central Universities (grant no. 14380122). Y.S. acknowledges the support from the Natural Science Foundation of Jiangsu Province (grant no. BK20150275).

AUTHOR CONTRIBUTIONS

J.Z., N.X., and P.Z. designed research. N.X., P.Z., and Y.S. performed research. N.X., P.Z., X.L., and L.Z. analyzed data. J.Z., N.X., P.Z., H.T., and S.Z. wrote the paper.

DECLARATION OF INTERESTS

The authors declare no competing interests

Received: October 15, 2019
Revised: November 21, 2019
Accepted: December 12, 2019
Published: January 10, 2020

REFERENCES

1. Mekonnen, M.M., and Hoekstra, A.Y. (2016). Four billion people facing severe water scarcity. Sci. Adv *2*, e1500323.
2. Mcilvaine, R. (2014). A new approach for evaluating energy choices. Electr. J. *27*, 72–79.
3. Schewe, J., Heinke, J., Gerten, D., Haddeland, I., Arnell, N.W., Clark, D.B., Dankers, R., Eisner, S., Fekete, B.M., Colón-González, F.J., et al. (2014). Multimodel assessment of water scarcity under climate change. Proc. Natl. Acad. Sci. USA *111*, 3245–3250.
4. Martin, C.L. (2013). Novel dry cooling technology for power plants (University of North Dakota Energy & Environmental Research Center). https://www.energy.gov/sites/prod/files/2014/01/f7/csp_review_meeting_042313_martin.pdf.
5. U.S. Department of Energy. (2017). Bandwidth study on energy use and potential energy savings opportunities in U.S. seawater desalination systems (U.S. Department of Energy). https://www.energy.gov/sites/prod/files/2017/12/f46/Seawater_desalination_bandwidth_study_2017.pdf.
6. Ammous, M., and Chaabene, M. (2015). Multi criteria sizing approach for photovoltaic thermal collectors supplying desalination plant. Energ. Convers. Manag *94*, 365–376.
7. Giwa, A., Fath, H., and Hasan, S.W. (2016). Humidification–dehumidification desalination process driven by photovoltaic thermal energy recovery (PV-HDH) for small-scale sustainable water and power production. Desalination *377*, 163–171.
8. Ong, C.L., Escher, W., Paredes, S., Khalil, A.S.G., and Michel, B. (2012). A novel concept of energy reuse from high concentration photovoltaic thermal (HCPVT) system for desalination. Desalination *295*, 70–81.
9. Polman, A., Knight, M., Garnett, E.C., Ehrler, B., and Sinke, W.C. (2016). Photovoltaic materials: present efficiencies and future challenges. Science *352*, aad4424.
10. Green, M.A., Hishikawa, Y., Dunlop, E.D., Levi, D.H., Hohl-Ebinger, J., and Ho-Baillie, A.W. (2018). Solar cell efficiency tables (version 52). Progress Photovoltaics *26*, 427–436.
11. Cariou, R., Benick, J., Feldmann, F., Höhn, O., Hauser, H., Beutel, P., Razek, N., Wimplinger, M., Bläsi, B., Lackner, D., et al. (2018). III–V-on-silicon solar cells reaching 33% photoconversion efficiency in two-terminal configuration. Nat. Energy *3*, 326–333.
12. National Renewable Energy Laboratory, https://www.nrel.gov/pv/assets/images/efficiency-chart.png.
13. Radziemska, E. (2003). The effect of temperature on the power drop in crystalline silicon solar cells. Renew. Energy *28*, 1–12.
14. Zhou, L., Tan, Y., Wang, J., Xu, W., Yuan, Y., Cai, W., Zhu, S., and Zhu, J. (2016). 3D self-assembly of aluminium nanoparticles for plasmon-enhanced solar desalination. Nat. Photon *10*, 393–398.
15. Ni, G., Zandavi, S.H., Javid, S.M., Boriskina, S.V., Cooper, T.A., and Chen, G. (2018). A salt-rejecting floating solar still for low-cost desalination. Energy Environ. Sci. *11*, 1510–1519.
16. Greenlee, L.F., Lawler, D.F., Freeman, B.D., Marrot, B., and Moulin, P. (2009). Reverse osmosis desalination: water sources, technology, and today's challenges. Water Res. *43*, 2317–2348.
17. Ghaffour, N., Missimer, T.M., and Amy, G.L. (2013). Technical review and evaluation of the economics of water desalination: current and future challenges for better water supply sustainability. Desalination *309*, 197–207.
18. Werber, J.R., Osuji, C.O., and Elimelech, M. (2016). Materials for next-generation desalination and water purification membranes. Nat. Rev. Mater *1*, 16018.
19. Alvarez, P.J.J., Chan, C.K., Elimelech, M., Halas, N.J., and Villagrán, D. (2018). Emerging opportunities for nanotechnology to enhance water security. Nat. Nanotechnol *13*, 634–641.
20. Chen, W., Chen, S., Liang, T., Zhang, Q., Fan, Z., Yin, H., Huang, K.W., Zhang, X., Lai, Z., and Sheng, P. (2018). High-flux water desalination with interfacial salt sieving effect in nanoporous carbon composite membranes. Nat. Nanotechnol *13*, 345–350.
21. Morelos-Gomez, A., Cruz-Silva, R., Muramatsu, H., Ortiz-Medina, J., Araki, T., Fukuyo, T., Tejima, S., Takeuchi, K., Hayashi, T., Terrones, M., et al. (2017). Effective NaCl and dye rejection of hybrid graphene oxide/graphene layered membranes. Nat. Nanotechnol *12*, 1083–1088.
22. Surwade, S.P., Smirnov, S.N., Vlassiouk, I.V., Unocic, R.R., Veith, G.M., Dai, S., and Mahurin, S.M. (2015). Water desalination using nanoporous single-layer graphene. Nat. Nanotechnol *10*, 459–464.
23. Elimelech, M., and Phillip, W.A. (2011). The future of seawater desalination: energy, technology, and the environment. Science *333*, 712–717.
24. U.S. Department of Energy. Bandwidth study U.S. seawater desalination systems. Department of Energy, https://www.energy.gov/eere/amo/downloads/bandwidth-study-us-seawater-desalination-systems.
25. Yang, P., Liu, K., Chen, Q., Li, J., Duan, J., Xue, G., Xu, Z., Xie, W., and Zhou, J. (2017). Solar-driven simultaneous steam production and electricity generation from salinity. Energy Environ. Sci. *10*, 1923–1927.
26. Zhu, L., Gao, M., Peh, C.K.N., Wang, X., and Ho, G.W. (2018). Self-contained monolithic carbon sponges for solar-driven interfacial water evaporation distillation and electricity generation. Adv. Energy Mater *8*, 1702149.
27. Neumann, O., Feronti, C., Neumann, A.D., Dong, A., Schell, K., Lu, B., Kim, E., Quinn, M., Thompson, S., Grady, N., et al. (2013). Compact solar autoclave based on steam generation using broadband light-harvesting nanoparticles. Proc. Natl. Acad. Sci. USA *110*, 11677–11681.
28. Neumann, O., Urban, A.S., Day, J., Lal, S., Nordlander, P., and Halas, N.J. (2013). Solar vapor generation enabled by nanoparticles. ACS Nano *7*, 42–49.
29. Ghasemi, H., Ni, G., Marconnet, A.M., Loomis, J., Yerci, S., Miljkovic, N., and Chen, G. (2014). Solar steam generation by heat localization. Nat. Commun *5*, 4449.
30. Zhang, L., Tang, B., Wu, J., Li, R., and Wang, P. (2015). Hydrophobic light-to-heat conversion membranes with self-healing ability for interfacial solar heating. Adv. Mater. *27*, 4889–4894.
31. Cui, L., Zhang, P., Xiao, Y., Liang, Y., Liang, H., Cheng, Z., and Qu, L. (2018). High rate production of clean water based on the combined photo-electro-thermal effect of graphene architecture. Adv. Mater *30*, e1706805.

32. Zhao, F., Zhou, X., Shi, Y., Qian, X., Alexander, M., Zhao, X., Mendez, S., Yang, R., Qu, L., and Yu, G. (2018). Highly efficient solar vapour generation via hierarchically nanostructured gels. Nat. Nanotechnol *13*, 489–495.

33. Chen, C., Li, Y., Song, J., Yang, Z., Kuang, Y., Hitz, E., Jia, C., Gong, A., Jiang, F., Zhu, J.Y., et al. (2017). Highly flexible and efficient solar steam generation device. Adv. Mater *29*, e1701756.

34. Xu, N., Li, J., Wang, Y., Fang, C., Li, X., Wang, Y., Zhou, L., Zhu, B., Wu, Z., Zhu, S., et al. (2019). A water lily–inspired hierarchical design for stable and efficient solar evaporation of high-salinity brine. Sci. Adv. *5*, eaaw7013.

35. Dongare, P.D., Alabastri, A., Pedersen, S., Zodrow, K.R., Hogan, N.J., Neumann, O., Wu, J., Wang, T., Deshmukh, A., Elimelech, M., et al. (2017). Nanophotonics-enabled solar membrane distillation for off-grid water purification. Proc. Natl. Acad. Sci. USA *114*, 6936–6941.

36. Hogan, N.J., Urban, A.S., Ayala-Orozco, C., Pimpinelli, A., Nordlander, P., and Halas, N.J. (2014). Nanoparticles heat through light localization. Nano Lett. *14*, 4640–4645.

37. Song, C., Li, T., Guo, W., Gao, Y., Yang, C., Zhang, Q., An, D., Huang, W., Yan, M., and Guo, C. (2018). Hydrophobic $Cu_{12}Sb_4S_{13}$-deposited photothermal film for interfacial water evaporation and thermal antibacterial activity. New J. Chem. *42*, 3175–3179.

38. Zhu, L., Gao, M., Peh, C.K.N., and Ho, G.W. (2018). Solar-driven photothermal nanostructured materials designs and prerequisites for evaporation and catalysis applications. Mater. Horiz *5*, 323–343.

39. Czanderna, A.W., and Pern, F.J. (1996). Encapsulation of PV modules using ethylene vinyl acetate copolymer as a pottant: a critical review. Sol. Energetic Mater. Sol. Cells *43*, 101–181.

40. Kim, J.A., Seong, D.G., Kang, T.J., and Youn, J.R. (2006). Effects of surface modification on rheological and mechanical properties of CNT/epoxy composites. Carbon *44*, 1898–1905.

41. Lacour, S.P., Jones, J., Wagner, S., Li, Teng, and Suo, Zhigang (2005). Stretchable interconnects for elastic electronic surfaces. Proc. IEEE *93*, 1459–1467.

42. Rogers, J.A., Someya, T., and Huang, Y. (2010). Materials and mechanics for stretchable electronics. Science *327*, 1603–1607.

43. WHO. (2011). Safe drinking-water from desalination. http://www.who.int/water_sanitation_health/publications/desalination_guidance/en/.

44. Chu, S., Cui, Y., and Liu, N. (2016). The path towards sustainable energy. Nat. Mater. *16*, 16–22.

45. Xu, X., Chen, J., Zhou, J., and Li, B. (2018). Thermal conductivity of polymers and their nanocomposites. Adv. Mater *30*, e1705544.

46. Zhang, P., Yuan, P., Jiang, X., Zhai, S., Zeng, J., Xian, Y., Qin, H., and Yang, D. (2018). A theoretical review on interfacial thermal transport at the nanoscale. Small *14*, 1702769.

47. Alsheghri, A., Sharief, S.A., Rabbani, S., and Aitzhan, N.Z. (2015). Design and cost analysis of a solar photovoltaic powered reverse osmosis plant for Masdar Institute. Energy Procedia *75*, 319–324.

48. Shalaby, S.M. (2017). Reverse osmosis desalination powered by photovoltaic and solar Rankine cycle power systems: a review. Renew. Sustain. Energy Rev. *73*, 789–797.

49. Duan, W., Yuan, S., Sheng, Y., Cai, W., Chen, Y., Yang, Y., Altermatt, P.P., Feng, Z., and Verlinden, P.J. (2016). A route towards high efficient N-type pert solar cells. 32nd European Photovoltaic Solar Energy Conference and Exhibition. https://www.researchgate.net/profile/Yifeng_Chen4/publication/307638554_A_ROUTE_TOWARDS_HIGH_EFFICIENCY_N-TYPE_PERT_SOLAR_CELLS/links/57ce5aac08ae83b37460ec7b.pdf

50. Han, F., Meng, G., Xu, Q., Zhu, X., Zhao, X., Chen, B., Li, X., Yang, D., Chu, Z., and Kong, M. (2011). Alumina-sheathed nanocables with cores consisting of various structures and materials. Angew. Chem. Int. Ed. Engl. *50*, 2036–2040.

51. Zhao, X., Meng, G., Xu, Q., Han, F., and Huang, Q. (2010). Color fine-tuning of CNTs@AAO composite thin films via isotropically etching porous AAO before CNT growth and color modification by water infusion. Adv. Mater *22*, 2637–2641.